

Monthly Weather Review

Quality of the Target Area for Metrics with Different Nonlinearity in a Mesoscale Convective System --Manuscript Draft--

Manuscript Number:	MWR-D-13-00244
Full Title:	Quality of the Target Area for Metrics with Different Nonlinearity in a Mesoscale Convective System
Article Type:	Article
Corresponding Author:	Zhiyong Meng School of Physics, Peking University Beijing , CHINA
Corresponding Author's Institution:	School of Physics, Peking University
First Author:	Ling Huang
Order of Authors:	Ling Huang Zhiyong Meng
Abstract:	<p>A direct piece-by-piece data assimilation targeting strategy through observing system simulation experiments was used to examine the quality of the target area for forecast metrics with different nonlinearity in a mesoscale convective vortex-associated rainfall event from both a deterministic and probabilistic perspective.</p> <p>The target area was determined based on the impact of assimilating synthetic wind-profiler observations, piece-by-piece, on the forecast error of strongly nonlinear rainfall and weakly nonlinear total energy around the initial vortex center. The quality of the target area in terms of its effectiveness and variability was examined for members of a reasonable ensemble. Apparently different target areas were found for different members, even for those with very small differences for both forecast metrics, with a larger variability observed for rainfall than for total energy. This result indicated that target areas estimated in deterministic scenarios are likely unreliable.</p> <p>Probabilistic target areas were created by averaging data-impact index values over the ensemble. Significant differences were also observed in the ensemble-based target areas for rainfall and total energy. For total energy, assimilating data in an inaccurate target area could decrease the forecast error at a similar magnitude as that in the target area. For rainfall, however, much less error reduction was obtained, the magnitude of which was almost comparable to the no-data-assimilation experiment. Overall, the results of this study suggest that designing a particular observation plan based on an estimated target area could be unnecessary for total energy and useless for rainfall, given the difficulty involved in accurately determining a target area in an operational setting.</p>

1 Quality of the Target Area for Metrics with Different Nonlinearity in a Mesoscale

2 Convective System

3

4 Ling Huang and Zhiyong Meng

5 Laboratory for Climate and Ocean-Atmosphere Studies, Department of Atmospheric

6 and Oceanic Sciences, School of Physics, Peking University, Beijing, China

7

8

9

10

11

12

13

14

15

16

To be submitted to Monthly Weather Review for Publication

17

Feb.12, 2014

18

19 Corresponding author address: Dr. Zhiyong Meng, Laboratory for Climate and

20 Ocean-Atmosphere Studies, Department of Atmospheric and Oceanic Sciences,

21 School of Physics, Peking University, Beijing, China.

22 E-mail: zymeng@pku.edu.cn

23

1 **Abstract**

2 A direct piece-by-piece data assimilation targeting strategy through observing
3 system simulation experiments was used to examine the quality of the target area for
4 forecast metrics with different nonlinearity in a mesoscale convective
5 vortex-associated rainfall event from both a deterministic and probabilistic
6 perspective.

7 The target area was determined based on the impact of assimilating synthetic
8 wind-profiler observations, piece-by-piece, on the forecast error of strongly nonlinear
9 rainfall and weakly nonlinear total energy around the initial vortex center. The quality
10 of the target area in terms of its effectiveness and variability was examined for
11 members of a reasonable ensemble. Apparently different target areas were found for
12 different members, even for those with very small differences for both forecast
13 metrics, with a larger variability observed for rainfall than for total energy. This result
14 indicated that target areas estimated in deterministic scenarios are likely unreliable.

15 Probabilistic target areas were created by averaging data-impact index values
16 over the ensemble. Significant differences were also observed in the ensemble-based
17 target areas for rainfall and total energy. For total energy, assimilating data in an
18 inaccurate target area could decrease the forecast error at a similar magnitude as that
19 in the target area. For rainfall, however, much less error reduction was obtained, the
20 magnitude of which was almost comparable to the no-data-assimilation experiment.
21 Overall, the results of this study suggest that designing a particular observation plan
22 based on an estimated target area could be unnecessary for total energy and useless
23 for rainfall, given the difficulty involved in accurately determining a target area in an
24 operational setting.

25

1 **1. Introduction**

2 Targeted observation, or adaptive observation, is a process that estimates areas
3 where assimilated additional observations would substantially reduce forecast error.
4 Targeted observation has been an active research topic since it was first proposed
5 (Snyder 1996). Targeting strategies can be roughly grouped into two categories,
6 including adjoint sensitivity or singular vector (e.g., Buizza and Palmer 1995;
7 Langland and Rohaly 1996; Pu et al. 1997; Palmer et al. 1998; Gelaro et al. 2002;
8 Coutinho et al. 2004; Wu et al. 2007b), and ensemble-based methods (e.g., Bishop
9 and Toth 1999; Anderson 2001; Bishop 2001; Majumdar et al. 2002a,b; Hamill and
10 Snyder 2002; Ancell and Hakim 2007; Liu and Kalnay 2008). In addition to all the
11 above linear-based methods, Mu et al. (2003) proposed a conditional nonlinear
12 optimum perturbation (CNOP) method.

13 Shortly after the theory of targeted observation was proposed, a series of field
14 campaigns were launched for mid-latitude weather, such as the Fronts and Atlantic
15 Strom-Track Experiments (FASTEX; Joly et al. 1999) in 1997, North Pacific
16 Experiment (NORPEX) (Langland et al. 1999) in 1998, Winter Strom Reconnaissance
17 Program (WSR) (Szunyogh et al. 2000) since 1999, and North Atlantic THORPEX
18 Regional Campaign (NA-TReC; Mansfield et al. 2005) in 2003. In addition, tropical
19 cyclone targeting field programs were launched, such as the Dropwindsonde
20 Observations for Typhoon Surveillance near the Taiwan Region (DOTSTAR; Wu et al.
21 2005) since 2003, THORPEX Pacific Asian Regional Campaign (T-PARC; Aberson
22 2011) in 2008, and North Atlantic Hurricane Surveillance program (Aberson 2003)

1 since 1998. On average, the short-range forecast error has been reduced by 10% over
2 regional verification areas, with some cases showing reductions of up to 50%.
3 Forecast skill has been improved in about 70% of cases when additional data have
4 been assimilated into identified target areas (Langland 2005). These numbers certainly
5 show the positive contribution to reducing forecast error made by targeted
6 observations. However, the improvements in forecast skill demonstrated in field
7 experiments have been much lower than expected and more and more verification
8 studies are showing insignificant or neutral impact of targeted observations (e.g.,
9 Aberson 2002; Wu et al. 2007a; Chou et al. 2011; Hamill et al. 2013). Consequently,
10 it is important to revisit the limitations and issues involved in targeted observation.

11 To make a targeted observation successful, three conditions have to be satisfied
12 (Langland 2005): 1) the target area must be accurate; 2) the target area must be
13 adequately sampled; and 3) the assimilation of targeted observations must be able to
14 reduce the forecast error of the chosen metric. The accuracy of the target area, target
15 area sampling, quality of the background field, observation type and
16 representativeness, assimilation technique, and the numerical model can all influence
17 the impact of targeted observation (Aberson 2002, 2003, 2008; Reynolds and
18 Rosmond 2003; Langland 2005). Among these factors, the quality of the target area is
19 one of the most important, and should be assessed by its effectiveness and variability.
20 A target area can be regarded as ‘effective’ if the error of the concerned forecast
21 metric is decreased by a significantly larger magnitude through assimilating additional
22 observations in the target area rather than anywhere else. In addition, from a

1 probabilistic point of view, the variability of the target area obtained in equally
2 possible situations needs to be low.

3 The quality of the target area is closely related to the skill of targeting strategies.
4 A major issue in current targeting approaches that may compromise the quality of the
5 target area is that all current targeting strategies except CNOP involve significant
6 linear assumptions.

7

8 However, an atmospheric model is a nonlinear system. Different degrees of linear
9 assumption involved in targeting strategies may change the structure, magnitude, or
10 location of target areas, thus increasing its variability. For examples, Mu et al. (2009)
11 found substantial differences when they compared the target areas produced by CNOP
12 and first singular vectors (FSVs) for typhoon cases. A large variability in target area
13 was observed among different linear-based targeting strategies (e.g., Wu et al. 2009;
14 Ansell and Hakim 2007). Even for a single linear-based targeted observation strategy,
15 the location and magnitude of the target area could be very sensitive to the model
16 resolution (Ansell and Mass 2006), model physics, and basic-state trajectory (Ansell
17 and Mass 2008).

18 The variability of the target area would become even larger for a forecast metric
19 with stronger nonlinearity relative to a weakly nonlinear forecast metric that has been
20 used for almost all current targeting strategies. Synoptic-scale metrics may remain
21 quasi-linear longer than at smaller scales (Reynolds and Rosmond 2003). Majumdar
22 et al. (2002b) found that the total energy singular vector and ensemble transform

1 Kalman filter approaches produce substantial differences in the target area for smaller
2 scale target features. Xie et al. (2013), with accumulated rainfall as the forecast metric
3 for typhoon Morakot (2009), clearly demonstrated the limitation of using
4 ensemble-based sensitivity analysis in locating the target area, due to the strong
5 nonlinearity in the governing dynamics of the typhoon. Consequently, the quality of
6 the target area for forecast metrics with different nonlinearity needs to be examined
7 using a strategy that fully accounts for the features of nonlinear error growth.

8 Another issue of all current strategies is that they estimate the analysis and
9 forecast variance instead of the forecast error (Mu 2013). However, identifying an
10 area that can decrease the forecast error variance the most does not necessarily result
11 in the largest error reduction of the forecast metric concerned. It could be more
12 intuitive and direct if the target area can be detected based on the ultimate goal of
13 targeted observation, i.e., minimum forecast error, instead of minimum forecast
14 variance.

15 In the present reported study, we used an error-based targeting strategy that did
16 not possess a linear-error growth assumption to assess the quality of the target area for
17 forecast metrics with different nonlinearity from both a deterministic and probabilistic
18 perspective for a heavy rain event associated with a mesoscale convective vortex
19 (MCV) in South China in June 2008. The targeting strategy used was the one most
20 commonly used for assessing targeted observation; namely, data assimilation. We
21 used “brute force” assimilation of different observations, piece-by-piece, through an
22 observing system simulation experiment (OSSE) to quantify their fully nonlinear

1 impact on the forecast metric and identify the target area where high data-impact
2 index values were located.

3 This piece-by-piece data assimilation targeting method (PBPDA) has several
4 benefits: 1) it does not require any linear assumption; 2) it is error- rather than
5 variance-based; 3) any type and resolution of targeted data can be examined through
6 the OSSE method; and 4) the targeting strategy is totally consistent with the data
7 assimilation procedure, i.e., the detection of the target area is totally consistent with
8 its evaluation, which has been regarded important in targeted observation (Berliner et
9 al. 1999; Langland 2005). Although the method might be difficult to use operationally
10 due to its reliance on future observational data, our expectation was that it would be a
11 good approach to examine the theoretical concept of targeted observation. We used an
12 ensemble to examine the quality of the target areas for the forecast metrics with
13 different nonlinearity among different members in the deterministic approach, and the
14 quality of the ensemble-based target area from the statistical perspective.

15 The remainder of the paper is structured as follows. A synoptic overview of the
16 MCV case is given in section 2. Section 3 introduces the PBPDA targeting strategy,
17 the OSSE procedures, and the forecast metric calculation. The results of the control
18 experiment, i.e., without data assimilation, are reported in section 4. Section 5
19 discusses the quality of the target area determined through PBPDA for strongly
20 nonlinear rainfall and weakly nonlinear total energy (TE). And finally, a summary and
21 discussion are presented in section 6.

22

1 **2. Case overview**

2 The weather event we studied was a torrential rain event in Guangxi Province,
3 China (Fig. 1), on 12 June 2008, which was associated with an MCV that originated
4 from Sichuan Province in Southwest China. This kind of MCV is usually referred to
5 as a ‘southwest vortex’ (Tao and Ding 1981), which is a mesoscale cyclonic vortex
6 (with a horizontal radius of 300–500 km) that forms in the lower troposphere over
7 Southwest China. The formation of a southwest vortex is defined by the appearance of
8 a mesoscale cyclonic circulation and a closed isobar at 700 hPa (Lu and Chen 1993).
9 Southwest vortices are usually caused by the interaction between the terrain of the
10 Tibetan Plateau and the atmospheric circulation. They usually dissipate where they
11 form, seldom moving away from their origin (Duan 2006). That said, some southwest
12 vortices do move out to the east, and usually cause extensive and severe heavy rain
13 along their tracks (Tao and Ding 1981; Lu and Chen 1993; Chen et al. 2003; Fu et al.
14 2010). Eastward-moving MCVs have emerged as key weather systems that cause
15 torrential rain in summer over East China.

16 The southwest vortex in this study formed in south Sichuan Province at 0000
17 UTC 11 June 2008 (Fig. 1). It first moved to the southeast and then turned to the
18 northeast. During its lifetime, the vortex center (the cross in Fig. 2) remained in front
19 of or near to the base of a 500-hPa geopotential trough followed by a 500-hPa
20 temperature trough (Fig. 2), which is a favorable environment for the development of
21 upward motion. With the eastward movement of a short wave at 500 hPa from the
22 Tibetan Plateau (Figs. 2a, b), a low pressure system with closed contours of

1 geopotential height first appeared at 700 hPa over southern Sichuan Province at 1800
2 UTC 10 June (Fig. 3b). The streamline field showed a convergence center near the
3 low pressure center with increased relative vertical vorticity, but no apparent cyclonic
4 circulation at this moment at 700 hPa. The cyclonic circulation became apparent at
5 0000 UTC 11 June together with a closed isobar at 700 hPa (Fig. 3c), which featured
6 the formation of the vortex. The vortex then intensified, expanded, matured at 1800
7 UTC 12 June over northern Guangxi Province (Figs. 3d, e), and dissipated over
8 Jiangxi Province after 0000 UTC 13 June.

9 The MCV lasted for 2 days and caused severe damage to Guangxi Province.
10 Almost half of Guangxi Province was covered by a 24-h rainfall event of >100 mm
11 [shading in Fig. 1; the observed rainfall data were provided by the China
12 Meteorological Administration (CMA)]. The 24-h accumulated rainfall during 0000
13 UTC 12 June – 00Z 13 June 2008 (hereafter referred to as $RAIN_{24}$) reached as much
14 as 250 mm in northern Guangxi (Fig. 1). Around 1.6 million people in 35 counties of
15 Guangxi Province were affected by this torrential rain event (Fu et al. 2010).

16

17 3. Methodology

18 a. *The PBPDA method for targeted observation*

19 A schematic representation of the PBPDA targeting strategy is depicted in Fig. 4.
20 The final analysis (FNL) of the Global Forecast System (GFS) of the NCEP at 0000
21 UTC 11 June was perturbed to generate an initial ensemble. The whole ensemble was
22 then integrated for 48 h. The member that best approximated the observed MCV flow

1 and $RAIN_{24}$ was used as the “truth” to generate synthetic observations by adding in
2 typical observation error. Then, in a given area around the initial MCV of the truth,
3 synthetic observations were grouped into small data units. By individually
4 assimilating each data unit into the initial field of the other ensemble members using
5 3DVar (Barker et al. 2004) followed by a 48-h simulation, the impact of assimilating
6 each data unit on the forecast error of certain forecast metrics relative to the control
7 (no data assimilation) experiment could be determined. 3DVar was used due to its
8 high efficiency, ease of implementation, and generally good performance (Hsiao et al.
9 2012; Gao et al. 2013). The distribution of the data-impact index could then clearly
10 show the possible target area. To make the analysis of the results easier, we divided
11 the range of positive data-impact index values into four levels and set all negative
12 values as zero. The target area of each member was then defined by the relatively
13 localized and compact area with high data-impact index values.

14 The model used in this study was the advanced research core of the Weather
15 Research and Forecasting model (WRF), version 3.2 (Skamarock and Klemp 2008).
16 The vertical coordinate follows the terrain using hydrostatic pressure, and the model
17 uses an Arakawa C grid. Prognostic variables are column mass of dry air (μ_d),
18 velocity (u , v , and w), potential temperature (θ), geopotential (ϕ), and mixing ratios
19 for water vapor (q_v), cloud water (q_c), rain (q_r), ice (q_i), snow (q_s), and graupel (q_g).
20 The model was run with two-way grid nesting. The coarse and fine-grid domains
21 respectively have horizontal grid sizes of 40.5 km and 13.5 km, and grid points of
22 150×120 and 181×136 (Fig. 5). There are 27 layers in the vertical direction, with a top

1 level at 100 hPa. Both domains use the WRF double-moment 6-class microphysics
2 scheme (Hong et al. 2004), the RRTMG long-wave radiation scheme (Mlawer et al.,
3 1997), the Yonsei University Planetary Boundary Layer scheme (Hong et al. 2006),
4 and the Grell–Devenyi ensemble cumulus parameterization scheme (Grell and
5 Devenyi 2002). The initial and boundary conditions were provided by the FNL/NCEP
6 dataset, which has a time interval of 6 h and a horizontal resolution of $1^\circ \times 1^\circ$.

7

8 *b. OSSE configuration*

9 A 48-h ensemble forecast was first performed with an ensemble size of 40 from
10 0000 UTC 11 to 0000 UTC 13 June 2008. The initial ensemble was generated with
11 WRF-3DVar (Barker et al. 2004) by adding perturbations randomly sampled from the
12 default background error covariance of “cv3” with the FNL analysis error as the
13 standard deviation. The background error covariance of “cv3” was generated through
14 the National Meteorological Center (NMC) method of averaged forecast differences
15 (Parrish and Derber 1992; Barker et al. 2004). The random perturbations were
16 generated initially for control variables (namely stream function, unbalanced velocity
17 potential, unbalanced surface pressure, unbalanced temperature, and “pseudo” relative
18 humidity) with a normal distribution (zero mean and unit standard deviation). The
19 perturbations of the control variables were then transformed into those of the model
20 prognostic variables via empirical orthogonal function (EOF) transformation, a
21 recursive filter, and physical transformation. The perturbed variables included the
22 horizontal wind components, potential temperature, and mixing ratio for water vapor.

1 Other prognostic variables, such as vertical velocity (w) and mixing ratios for cloud
2 water (q_c), rainwater (q_r), snow (q_s), and graupel (q_g), were not perturbed. The
3 domain-averaged standard deviation of these perturbations was 2.16 m s^{-1} for u , 2.42
4 m s^{-1} for v , 0.99 K for T , 1 hPa for pressure perturbation (p'), and 0.77 g kg^{-1} for q_v .
5 This method of generating the initial ensemble has also been used in many other
6 studies (e.g., Houtekamer et al. 2005; Barker 2005; Zhang et al. 2006; Meng and
7 Zhang 2007, 2008a,b, 2011; Wu et al. 2013).

8 The targeted observations were synthetic wind profilers. Wind profilers measure
9 wind speed and wind direction at various elevations above the ground. Compared
10 with rawinsonde, wind profilers have the advantage of higher temporal and vertical
11 resolution with a fully automatic operation. They are not affected by air traffic control
12 since they do not need an air balloon. Wind profilers are becoming widely used to fill
13 the spatial and temporal gap of rawinsonde observations.

14 The synthetic wind profilers were generated by adding observation error to the
15 “truth” (Figs. 6c1–3), an ensemble member whose simulation was the most
16 comparable to FNL analyses in terms of the location and intensity of the MCV (Fig.
17 6a1), and to observations in terms of its associated composite radar reflectivity at its
18 mature stage (1800 UTC 12 June, provided by the CMA) (Fig. 6a2) and $RAIN_{24}$ (Fig.
19 6a3). We assumed that the synthetic profiler winds had independent Gaussian errors
20 with zero mean and a standard deviation as per the default in the WRF-3DVar
21 pre-processing package (Table 1), which has been used previously by Meng and
22 Zhang (2008a) for examining the relative performance of assimilating different

1 observation platforms. To emulate the characteristics of the real-world wind-profiler
2 observations, the limitations of wind profilers, such as impact from ground clutter,
3 and inaccuracy both in rain and within 500 m above the ground (Zhang 2011, personal
4 communication) were also taken into account. The observations under the surface and
5 within 500 m above the ground were removed. Furthermore, the wind speed needed to
6 be larger than 5.97 m s^{-1} so that the error of wind direction was within 10° (Chen and
7 Wang 2000).

8 The area within which synthetic observations were generated was determined
9 based on the general size of the target area of TCs, because no literature exists on
10 targeting observations for MCVs. The target area of a TC is generally within a radius
11 of 500–1000 km from the TC center (e.g., Majumdar et al. 2006; Wu et al. 2007b,
12 2009; Yamaguchi et al. 2009; Mu et al. 2009; Harnisch and Weissmann 2010; Qin and
13 Mu 2011; Aberson et al. 2011; Kim et al. 2011). Since MCVs are generally equivalent
14 to small and weak TCs, we selected a square of sides 1100 km in domain 1 with the
15 center of the initial MCV slightly to the southeast of the square's center (marked in
16 Fig. 3c) in order to cover more upstream area. Each data unit was a small square that
17 consisted of nine neighboring grid points, and thus had sides of 121.5 km (the small
18 squares in the dashed box in the middle of Fig. 4; an enlarged example is shown in
19 Fig. 7). There were a total of 81 units in the selected square area. Through
20 unit-by-unit data assimilation, 81 experiments were performed for each member,
21 consisting of initial one-unit data assimilation and a subsequent 48-h forecast. The
22 impact of individual data units was then assessed for the chosen forecast metrics,

1 described as follows.

2

3 *c. Forecast metrics*

4 Two forecast metrics were explored in this work, with different degrees of
5 nonlinearity. The first was $RAIN_{24}$, which is strongly nonlinear, and the other was
6 synoptic-scale wind and temperature in terms of TE , which is weakly nonlinear.

7 To determine the target area of $RAIN_{24}$, where assimilating synthetic profiler
8 winds provided greater improvement than other areas, we designed an index based on
9 the threat score (TS) of forecasted $RAIN_{24}$ that exceeded 50 mm in domain 2:

$$10 \quad R = \frac{TS_{DA} - TS_{NoDA}}{TS_{NoDA}}, \quad (1)$$

11 where TS_{DA} and TS_{NoDA} denote the TS of $RAIN_{24}$ with and without data assimilation,
12 respectively. A larger R index denotes a greater contribution from the assimilated
13 observation. The impact of data assimilation on the less-nonlinear TE was determined
14 by an index based on the mean DTE of domain 2:

$$15 \quad F = \frac{DTE_{NoDA} - DTE_{DA}}{DTE_{NoDA}}, \quad (2)$$

16 in which DTE is the difference total energy (Zhang et al. 2003) that reflects the
17 overall error of U , V and T :

$$18 \quad DTE = \frac{1}{2} \sum (U'_{ijk}{}^2 + V'_{ijk}{}^2 + \kappa T'_{ijk}{}^2) \quad (3)$$

19 where U' , V' , T' are the difference between a given member and the “truth”,
20 $\kappa = C_p / T_r$ ($C_p = 1004.9 \text{ J kg}^{-1} \text{ K}^{-1}$, $T_r = 287 \text{ K}$), and i, j, k are the index of x, y, z
21 coordinates, respectively.

1

2 *d. Determination of the target area*

3 To examine the target area quantitatively, the positive data-impact index was
4 categorized into four levels (e.g., the R index distribution for member 27, as shown in
5 Fig. 7). The area covered by the data units with the highest level of data-impact index
6 was defined as a target area if it was limited or localized enough to satisfy the
7 following two criteria: 1) the number of data units (denoted by N_u) were no larger
8 than 30% of the total 81 data units; namely, $N_u \leq 24$; and 2) $N_p + N_s \leq 10$, in which N_p
9 denotes the number of area with connected pieces of these data units ('connected'
10 means either sharing a same side or a same point), and N_s denotes the least number of
11 sides of the data unit square that connects different pieces. A larger $N_p + N_s$ denotes a
12 less-localized target area. These criteria were trial-and-error based through eyeball
13 examination. For example, the highest level of R index of member 27 was L4 (Fig. 7):
14 $N_u = 15 \leq 24$, $N_p = 3$, $N_s = 4$, $N_p + N_s = 7 \leq 10$. Consequently, the target area for
15 $RAIN_{24}$ for this member was established as the area marked in orange in Fig. 7.

16

17 **4. Control experiments**

18 *a. Deterministic forecast*

19 Initiated directly from the FNL data at 0000 UTC 11 June, the WRF produced a
20 decent simulation of the MCV, its radar reflectivity, and associated $RAIN_{24}$ (Figs.
21 6a–b). The location of the simulated circulation center at 1800 UTC 12 June (Fig. 6b1)
22 lay about 50 km to the southwest of the analysis (Fig. 6a1) with a slightly stronger

1 intensity in terms of maximum vertical vorticity at 700 hPa. The observed radar
2 reflectivity at 1800 UTC 12 June (Fig. 6a2) had a maximum value in northeastern
3 Guangxi, which was well captured by the model (Fig. 6b2). The simulated $RAIN_{24}$
4 (Fig. 6b3) approximated the observed heavy rainfall over northern Guangxi Province,
5 reaching as much as 250 mm (Fig. 6a3). Consequently, the WRF model with current
6 configuration was able to successfully simulate the evolution of both the MCV and its
7 rainfall.

8

9 *b. The ensemble forecast*

10 The performance of the ensemble forecast in terms of $RAIN_{24} > 50$ mm was
11 examined via the TS against the observation in domain 2. The results showed that six
12 members (15%) successfully captured the rainfall with a $TS > 0.3$. Twelve members
13 (30%) had a TS of 0.2–0.3. The remaining members, which produced poor rainfall
14 forecasts, accounted for 55% of all members. Thus, the performance of the ensemble
15 was generally reasonable.

16 The evolutions of the DTE of the 39 members are plotted in Fig. 8a. Since our
17 aim was to explore the features of the target areas among different ensemble members
18 that were almost equally likely, we trimmed the ensemble by dropping six outliers,
19 including M16, which had the largest initial DTE , and M13, M17, M36, M37, and
20 M40, which had the smallest initial DTE . The remaining less-scattered 33 members
21 comprised the working ensemble whose results are examined in the rest of the paper
22 (Fig. 8b).

1

2 5. Quality of the target area

3 a. The strongly nonlinear metric: $RAIN_{24}$

4 1) Deterministic approach

5 The distribution of R index of all 33 of the members is demonstrated in Fig. 9.

6 Target areas were detected in about 45% of the ensemble (denoted by black numbers).

7 The effectiveness of the target area was examined through comparing the error of the

8 forecast metric by assimilating all the data units in the detected target area into the

9 initial field, to that by assimilating the same amount of data units but in a different

10 area. We used M27 as an example to calculate the TS of forecasted $RAIN_{24}$ by

11 assimilating all the 15 data units in the target area (0.11 in Fig. 10). Then, the

12 experiment was repeated five times by assimilating the same number of data units but

13 with a random distribution in the data square, as shown in Fig. 10. The median of the

14 TS of the five realizations of randomly distributed data was used to denote the impact

15 of assimilating random observations (0.08 in Fig. 10). First, the TS with targeted data

16 assimilation was significantly higher than that without data assimilation (NoDA).

17 Second, the TS with target data assimilation was significantly higher than that with

18 random data assimilation. In other words, assimilating the targeted observations

19 substantially improved the forecast of $RAIN_{24}$ compared to assimilating the same

20 amount of data but with a random distribution. Consequently, the target area was

21 effective. Third, the TS with random data assimilation was apparently higher than that

22 of NoDA. This result indicates that a certain amount of forecast error could still be

1 decreased even when the estimated target area was substantially inaccurate, although
2 the reduced error was not as large as that obtained with an accurate target area.

3 Significant differences were observed in the magnitude, structure and location of
4 the target area of $RAIN_{24}$ among the different members (Fig. 9), indicating a large
5 variability of the target area. The magnitude of the target area ranged from L1 to L4.
6 The number of data units in the target area varied from zero to 24. The location of the
7 target area was scattered all over the domain, such as to the south (M27), northwest
8 (M4), around (M34), north (M2) or southwest (M11) of the vortex center, with
9 different degrees of compactness varying from tightly connected (e.g., M4) to widely
10 separated (e.g., M33).

11 Substantially different target areas were even found in members very close to
12 each other in terms of both forecast fields and their DTE . For example, M3 and M27
13 were very similar to each other in terms of forecasted $RAIN_{24}$, the patterns of the MCV,
14 and their vertical vorticities and radar reflectivities at the mature stage (Figs. 6d, e).
15 The absolute error of initial T , vertical vorticity and horizontal wind speed at 700 hPa,
16 the magnitude and evolution of volume-averaged DTE (Figs. 11a, b), and their
17 horizontal distribution of vertically-averaged DTE at the initial and end times were
18 also similar (Fig. 8b). However, there were no data units of L4 in M3, and only one
19 data unit reached L2 to the northwest of the MCV center (Fig. 11a1); while in M27 a
20 target area with L4 was mainly located to the south of the MCV center (Fig. 11b1).

21 M6 and M30 were even closer to each other relative to M3 and M27 in terms of
22 volume-averaged DTE , with almost the same magnitude at the initial time (Fig. 8b)

1 and a more similar horizontal pattern of vertically-averaged *DTE* as well as absolute
2 error of initial *T*, vertical vorticity, and horizontal wind speed (Figs. 11c, d). Their
3 simulated *RAIN*₂₄, patterns of the MCV, and their vertical vorticities and radar
4 reflectivities at the mature stage were also very similar (Figs. 6f, g). However,
5 significant differences were found in their target area features (Figs. 11c1, d1). M30
6 displayed a feature similar to M3, with a target area located to the northwest of the
7 MCV center, while the data units of its highest L2 in M6 were too scattered to meet
8 the criteria of target area (Fig. 11c1; $N_p = 4$, $N_s = 13$, $N_p + N_s = 17 > 10$).

9 The above results demonstrate that small differences in the initial field may make
10 a big difference in terms of the data impact, and consequently in the existence and the
11 location, structure and magnitude of the target area. The fact that different members
12 produced apparently different locations of the target area suggests that the target area
13 of a strongly nonlinear forecast metric cannot be determined through the deterministic
14 method.

15

16 2) Probabilistic approach

17 With the huge variability of the target area among different ensemble members in
18 mind, we subsequently examined the possibility of determining the target area from a
19 probabilistic point of view. With all the negative *R* index values in the 33 members set
20 to zero, the ensemble mean *R* index was calculated (Fig. 12a). The data units with
21 high *R*-index values were located mainly in a southwest–northeast oriented zone with
22 three pieces of data units of L4. The L4 data units were so scattered that they barely

1 met the criteria of the target area ($N_p = 3$, $N_s = 7$, $N_p + N_s = 10$). Four of the five data
2 units of the target area were located to the southwest of the MCV center, which
3 suggested that adding extra data into the southwest of the MCV center may
4 statistically improve the $RAIN_{24}$ forecast. The ensemble-based target area was
5 expected to be closer to the true target area and thus should be more statistically
6 accurate than the target area determined by individual members. Meanwhile, a large
7 variability of the target area among different members and a subsequent scattering of
8 data units in the ensemble-based target area would suggest that the target area for
9 highly-nonlinear rainfall was probably imprecise and thus possibly not very reliable.

10 The effectiveness of the ensemble-based target area was verified using a method
11 similar to that described in section 5a.1. The five observation units in the
12 ensemble-based target area shown in Fig. 12a were assimilated into the initial fields of
13 all 33 members. The mean of the TS of the forecasted $RAIN_{24}$ of the 33 members was
14 used to represent the impact of assimilating the data in the target area. Then, the
15 experiment was repeated five times by assimilating the same number of data units but
16 with a random distribution, as shown in Fig. 10. The median of the TS of the five
17 realizations of randomly distributed data was used to denote the impact of
18 assimilating random observations. The results showed that the ensemble-based target
19 area was effective as indicated by the significantly larger TS with targeted data
20 assimilation than that of random data assimilation and NoDA, which was the mean of
21 the TS of the 33 members without data assimilation. An interesting result was that the
22 TS with random data assimilation was not significantly different from that of NoDA,

1 which was apparently different from the result obtained using the deterministic
2 approach. This suggests that targeted observation for rainfall requires that the target
3 area is strictly accurate and adequately sampled to obtain a statistically positive effect.

4 Overall, the above results indicate that, for a forecast metric of rainfall that is
5 strongly nonlinear, the ensemble-based target area is effective but has a large
6 uncertainty. Considering the small possibility of obtaining an exactly accurate target
7 area beforehand in practice and the similar performance of random data assimilation
8 to NoDA, targeted observation for strongly nonlinear forecast metrics such as rainfall
9 may easily fail.

10

11 *b. The weakly nonlinear metric: total energy*

12 The distribution of F index for TE of all 33 members is demonstrated in Fig. 13.
13 About 64% of the ensemble had target areas that satisfied our criteria, which was
14 larger than that for rainfall. Although more members had target areas for TE relative
15 to $RAIN_{24}$, there was still apparently large variability in terms of the location, structure
16 and magnitude of target areas among the 33 members, such as the opposite direction
17 of location relative to the MCV center of M4 and M19, and the markedly different
18 magnitudes of M29 and M30.

19 The difference in the target area of the ensemble pairs that had similar MCV
20 features and initial, end values and evolution of DTE (M3 and M27, M6 and M30)
21 became less apparent for the forecast metric of TE (Figs. 11a2–d2). M6 had a target
22 area for TE with a very similar location as that of M30, though the magnitude was

1 apparently different. The location of the target area of M3 and M27 was still markedly
2 different, but much closer to each other than those for $RAIN_{24}$. An interesting result
3 was that the target areas of M3 and M27 for TE were almost in the opposite direction
4 relative to the MCV center compared to their counterparts for $RAIN_{24}$. This
5 phenomenon became less significant for the pair of M6 and M30, whose $DTEs$ were
6 slightly smaller. This result indicates that extra data assimilation that most efficiently
7 decreases the total error in TE does not guarantee the most efficient decrease of error
8 in the associated rainfall.

9 Together, these results show that, even though the variability of the target areas
10 was lower for TE , which has a weaker nonlinearity than $RAIN_{24}$, using a deterministic
11 approach to determine their target areas still could not guarantee a statistically
12 positive impact. Initial uncertainties may easily dislocate the target area and thus
13 compromise the improvement in forecast skill. This could be why some targeted
14 observation experiments do not obtain apparent improvement in their long-term
15 verification. The large variability in the target area for synoptic-scale metric was
16 noticed by Ansell and Mass (2008) using adjoint targeting method. Their results are
17 further confirmed by our work using a non-linear approach.

18 Using the probabilistic approach, the ensemble-based target area for TE was also
19 examined through calculating the mean F index of TE over the 33 ensemble members
20 (Fig. 12b). The high F index values were mainly located in a zone that was generally
21 northwest–southeast oriented, which was apparently different from the high-index
22 zone for $RAIN_{24}$. A perfectly compact target area was detected to the north of the

1 MCV center, with five connected L4 data units. The huge difference between the
2 location of the ensemble-based target area for $RAIN_{24}$ and TE further confirmed that
3 the extra data assimilation that most efficiently decreases the total error in the flow
4 and temperature pattern does not guarantee the most efficient decrease of error in the
5 associated rainfall.

6 The effectiveness of the ensemble-based target area for total energy was assessed
7 in the same way as for rainfall (Fig.10). The mean DTE was significantly smaller than
8 that of NoDA but not significantly different from that of random data assimilation,
9 indicating the ineffectiveness of the ensemble-based target area for TE . This result
10 suggests that, for targeted observation with TE as the forecast metric, the forecast
11 error is likely to be reduced by a similar magnitude no matter whether the target area
12 is accurate or not. This could be what was happening in the previously mentioned
13 field targeted observation campaigns, in which a 10% improvement of forecast skill
14 was obtained using linear-based targeting strategies for forecast metrics of
15 synoptic-scale, weakly nonlinear TE or typhoon track. The impact of these field
16 campaigns was usually verified by comparing the forecast error with and without the
17 assimilation of targeted observations. What was really assessed was the importance of
18 the additional data, but not the importance of all the efforts made to identify a
19 particular target area, as opposed to any other area.

20

21 *c. The possible role of forecast metric nonlinearity*

22 To examine the possible contribution of error growth during the forecast vs.

1 initial data assimilation to the distribution of data-impact index values and their
 2 associated target areas, the I index, which reflects the data impact on initial TE , was
 3 defined, similar to the F index, as:

$$4 \quad I = \frac{DTE_{NoDA} - DTE_{DA}}{DTE_{NoDA}}. \quad (4)$$

5 The distribution of I index values is shown in Fig. 14. The percentage of ensemble
 6 members with target area (76%) was slightly larger than that for the F index (64%),
 7 and both were apparently larger than that of the R index (45%) (Table 2).

8 The target area showed much less variability than for both the R and F indices,
 9 which was quantitatively shown by the standard deviation of their $N_p + N_s$, with
 10 values of 6.3, 3.4, and 2.1 for the R , F , and I indices, respectively (Table 2). The
 11 mean $N_p + N_s$ values for the R , F , and I indices were 5.4, 3.2, and 1.9, respectively
 12 (Table 2), indicating that the target area became more compact and thus showed less
 13 variability from R to F and I . The target area for the initial TE appeared mostly near
 14 or to the southeast of the MCV center. For the two pairs of ensemble members,
 15 which had similar initial, end values and evolution of DTE, their target areas showed
 16 even closer features (Figs. 11a3–d3). The target area of M3 and M27 were both to
 17 the east of the MCV center, with the target area of M27 covering more data units.
 18 M6 and M30, which had even more similar initial DTE , showed almost exactly the
 19 same target area, which was located to the south of the MCV center.

20 The target areas for TE at the initial time were generally different from the
 21 corresponding target areas for both rainfall and forecasted TE . This feature could be
 22 clearly seen in the location of their ensemble-based target areas (Fig. 12). The mean

1 *I* index showed a perfectly compact target area to the southeast of the MCV center. It
2 was substantially different from the target area based on the *F* index, located to the
3 north of the MCV center, and the target area based on the *R* index, which was
4 scattered with a dominant location to the southwest of the MCV center. The
5 difference in the target area for initial *TE* from those for forecasted rainfall and *TE*
6 suggested that nonlinear error growth might have played an important role in the
7 distribution of the target area for both strongly nonlinear rainfall and weakly
8 nonlinear *TE*. The additional data assimilation that was able to reduce the initial
9 *DTE* the most did not guarantee the largest error reduction in the forecasted *DTE*, let
10 alone rainfall. For weakly nonlinear forecast metrics, the variability of target areas
11 was smaller and thus resulted in a more compact target area. The weakly nonlinear
12 error growth seemed to change the location of the localized target area only, while
13 the strongly nonlinear error growth seemed to change both the location and
14 compactness of the target area.

15

16 6. **Summary and discussion**

17 In the present reported study, we examined the quality of the target area for two
18 forecast metrics with different nonlinearity (rainfall vs. *TE*) associated with an MCV
19 in Southwest China during 11–13 June 2008. The examination was performed from
20 both a deterministic and statistical perspective using the PBPDA method within the
21 framework of an OSSE. The quality of the target area was examined in terms of its
22 effectiveness and variability.

1 Data assimilation is a common way to assess the performance of targeted
2 observation. Through examining the direct impact of assimilating synthetic
3 observations, piece-by-piece, at the initial time by 3DVar on the reduction of the
4 forecast error of certain metrics, the target area was defined as the limited area with
5 the highest level of data-impact index values. This targeting method not only
6 accommodates fully nonlinear error evolution, thus avoiding the limitation of current
7 strategies with linear assumptions, but is also consistent with the data assimilation
8 method.

9 Results showed that the target area determined via the deterministic approach
10 was not quite reliable for both strongly nonlinear forecasted rainfall and weakly
11 nonlinear *TE*. Large variability was observed in terms of the location, structure and
12 magnitude of target areas among different equally-likely ensemble members with a
13 reasonable initial ensemble spread. Even those members that had very small
14 differences in their flow and rainfall simulations showed substantially different target
15 areas. The high sensitivity of the target area to the uncertainties of the initial field,
16 which were comparable to the analysis error, for both the strongly nonlinear
17 forecasted rainfall and the weakly nonlinear *TE*, indicates that target areas can be
18 easily misplaced in deterministic scenarios. Larger variability was seen in the target
19 area for rainfall among different members than for *TE*. Less ensemble members
20 produced target areas for rainfall than for *TE*. The target area for *TE* was also more
21 compact than that for rainfall. These results indicated that the target area for rainfall
22 was less reliable than that for *TE*.

1 Through averaging the data-impact index values of ensemble members, the
2 ensemble-based target area was obtained for both forecasted rainfall and *TE*. The data
3 units in the ensemble-based target area for rainfall were much more scattered, almost
4 failing to meet the criteria of the target area, as compared to that for *TE*, suggesting
5 less reliability. Analyses on the effectiveness of the ensemble-based target area
6 suggest that adding more data in a particular estimated target area, or in a random
7 distribution near the weather system concerned, can both decrease the forecast error
8 of *TE* by a similar magnitude, thus targeted observing may not be necessary. On the
9 other hand, the forecast error of rainfall tends to be markedly reduced only when the
10 data are added to an accurate target area. Since the target area for rainfall has less
11 precision due to its larger variability relative to that of *TE*, it is thus likely to be
12 difficult to estimate accurately in practice, and so targeted observation for rainfall may
13 easily fail.

14 The large variability of the target area for forecasted rainfall was mainly due to its
15 highly nonlinear error-growth feature. By comparing the target areas for forecasted
16 rainfall and *TE* with that for initial *TE*, it was found that target areas for forecasted
17 rainfall and *TE* were substantially different from that for initial *TE*. This result
18 indicates that assimilating extra data that may improve the initial flow and
19 temperature the most does not guarantee the greatest improvement in their forecast
20 skill, let alone their associated rainfall. The weak nonlinearity of *TE* seemed to only
21 change the location of the compact target area for the initial *TE*, while the strong
22 nonlinearity of rainfall seemed to change both the location and compactness of the

1 target area.

2 Finally, it is important to note that this study was based on one case using the
3 3DVar data assimilation method for synthetic wind-profiler observations. The results
4 obtained within an OSSE framework may not be fully applicable to real-world
5 situations. Using real-world satellite data to examine the quality of target areas is
6 worthy of examination in the future. Further work covering more cases, different
7 forecast metrics, data assimilation methods, synthetic observation platforms and sizes
8 of data units needs to be done to obtain more general conclusions. The direct
9 piece-by-piece data assimilation targeted observation strategy used in this study is an
10 ideal method to examine targeted observation in a theoretical context, but it is almost
11 impossible to apply it operationally since it requires future observations or “truth” to
12 work. Besides assessing the quality of the target area, this PBPDA targeting strategy
13 could also be used to verify the relative performance of various targeting observation
14 strategies.

15

16 **Acknowledgements**

17 We thank Fuqing Zhang from Pennsylvania State University and Mu Mu from the
18 Institute of Oceanology, Chinese Academy of Sciences for insightful suggestions. We
19 also greatly benefited from comments given by Yunji Zhang and Huizhen Yu from
20 Peking University. This research was sponsored by Ministry of Science and
21 Technology of China Grants 2013CB430104 and GYHY201306004, and China
22 NSF Grant 41075031 and 41130960.

1

2 **References**

3 Aberson, S. D., 2002: Two years of operational hurricane synoptic surveillance. *Wea.*
4 *Forecasting*, **17**, 1101–1110.

5 Aberson, 2003: Targeted observations to improve operational tropical cyclone track
6 forecast guidance. *Mon. Wea. Rev.*, 131, 1613–1628.

7 Aberson, S. D., 2008: Large forecast degradation due to synoptic surveillance during
8 the 2004 and 2005 hurricane seasons, *Mon. Wea. Rev.*, 139, 3138–3150.

9 Aberson S D. 2011. The impact of dropwindsonde data from the THORPEX pacific
10 area regional campaign and the NOAA hurricane field program on tropical
11 cyclone forecasts in the global forecast system. *Mon. Wea. Rev.*, **139**, 2689–2703

12 Aberson, S. D., S. J. Majumdar, C. A. Reynolds, B. J. Etherton, 2011: An observing
13 system experiment for tropical cyclone targeting techniques using the global
14 forecast system. *Mon. Wea. Rev.*, **139**, 895–907.

15 Ancell, B., and C. Mass, 2006: Structure, growth rates, and tangent linear accuracy of
16 adjoint sensitivities with respect to horizontal and vertical resolution. *Mon. Wea.*
17 *Rev.*, **134**, 2971–2988.

18 Ancell, B., and G. J. Hakim, 2007: Comparing adjoint- and ensemble sensitivity
19 analysis with applications to observation targeting. *Mon. Wea. Rev.*, **135**,
20 4117–4134.

21 Ancell, B., and C. Mass, 2008: The variability of adjoint sensitivity with respect to
22 model physics and basic-state trajectory. *Mon. Wea. Rev.*, **136**, 4612–4628. Ancell,

- 1 B. and G. Hakim, 2007: Comparing adjoint- and ensemble-sensitivity analysis
2 with applications to observation targeting. *Mon. Wea. Rev.*, **135**, 4117–4134
- 3 Anderson, J., 2001: An ensemble adjustment Kalman filter for data assimilation. *Mon.*
4 *Wea. Rev.*, **129**, 2884–2903.
- 5 Barker, D., W. Huang, Y. Guo, A. Bourgeois, and Q. Xiao, 2004: A three-dimensional
6 variational data assimilation system for MM5: Implementation and initial results.
7 *Mon. Wea. Rev.*, **132**, 897–914.
- 8 Barker, D., 2005: Southern high-latitude ensemble data assimilation in the Antarctic
9 Mesoscale Prediction System. *Mon. Wea. Rev.*, **133**, 3431–3449.
- 10 Berliner, L. M., Z. Lu, and C. Snyder, 1999: Statistical design for adaptive weather
11 observations. *J. Atmos. Sci.*, **56**, 2536–2552.
- 12 Bishop, C., and Z. Toth, 1999: Ensemble transformation and adaptive observations. *J.*
13 *Atmos. Sci.*, **56**, 1748–1765.
- 14 Bishop, C., B. Etherton and S. Majumdar, 2001: Adaptive sampling with the ensemble
15 transform Kalman filter. Part I: Theoretical aspects. *Mon. Wea. Rev.*, **129**,
16 420–436.
- 17 Buizza, R., and T. Palmer, 1995: The singular-vector structure of the atmospheric
18 global circulation. *J. Atmos. Sci.*, **52**, 1434–1456.
- 19 Chen Z., M. Xu, W. Min, Q. Miao, 2003: Relationship between abnormal activities of
20 southwest vortex and heavy rain the upper reach of Yangtze river during summer
21 of 1998, *Plateau Meteorology*, **22**, 162–167. (In Chinese with English abstract)
- 22 Chou, K., C. Wu, P. Lin, S. Aberson, M. Weissmann, F. Harnisch and T. Nakazawa,

- 1 2011: The impact of dropwindsonde observations on typhoon track forecasts in
2 DOTSTAR and T-PARC, *Mon. Wea. Rev.*, **139**, 1728–1743.
- 3 Coutinho, M., J., Hoskins, and R., Buizza, 2004: The influence of physical processes
4 on extratropical singular vectors. *J. Atmos. Sci.*, **61**, 195–209.
- 5 Duan, L., 2006: Relationship between frequency of moving direction of southwest
6 vortex and rainfall in flood season, *Meteorology Monthly*, **32**, 23–27. (In Chinese
7 with English abstract)
- 8 Fu, S. M., S. Zhao, J. Sun, and W. Li, 2010: One kind of vortex causing heavy rainfall
9 during pre-rainy season in South China, *Chinese Journal of Atmospheric
10 Sciences*, **34** (2), 235–252. (in Chinese with English Abstract)
- 11 Gelaro, R., Rosmond, T. and Daley, R. 2002: Singular vector calculations with an
12 analysis error variance metric. *Mon. Wea. Rev.*, **130**, 1166–1186
- 13 Gao, Jidong, and Coauthors, 2013: A real-time weather-adaptive 3DVAR analysis
14 system for severe weather detections and warnings. *Wea. Forecasting*, **28**,
15 727–745.
- 16 Grell, G, and D. Devenyi, 2002: A generalized approach to parameterizing convection
17 combining ensemble and data assimilation techniques. *Geophys. Res. Lett.*,
18 **29(14)**, doi: 10.1029/2002GL015311.
- 19 Hamill, T., and C. Snyder, 2002: Using improved background-error covariances from
20 an ensemble Kalman filter for adaptive observations. *Mon. Wea. Rev.*, **130**,
21 1552–1572.
- 22 Hamill, T., F. Yang, C. Cardinali and S. Majumdar, 2013: Impact of targeted winter

1 storm reconnaissance dropwindsonde data on midlatitude numerical weather
2 predictions. *Mon. Wea. Rev.*, **141**, 2058–2065.

3 Harnisch, F., M. Weissmann, 2010: Sensitivity of typhoon forecasts to different
4 subsets of targeted dropsonde observations. *Mon. Wea. Rev.*, **138**, 2664–2680.

5 Hsiao, Ling-Feng, Der-Song Chen, Ying-Hwa Kuo, Yong-Run Guo, Tien-Chiang Yeh,
6 Jing-Shan Hong, Chin-Tzu Fong, Cheng-Shang Lee, 2012: Application of WRF
7 3DVAR to operational typhoon prediction in Taiwan: Impact of outer loop and
8 partial cycling approaches. *Wea. Forecasting*, **27**, 1249–1263.

9 Hong, S., J. Dudhia, and S. Chen, 2004: A revised approach to ice microphysical
10 processes for the bulk parameterization of clouds and precipitation. *Mon. Wea.*
11 *Rev.*, **132**, 103–120.

12 Hong, S., Y. Noh, and J. Dudhia, 2006: A new vertical diffusion package with an
13 explicit treatment of entrainment processes. *Mon. Wea. Rev.*, **134**, 2318–2341.

14 Houtekamer, P., and H. Mitchell, G. Pellerin, M. Buehner, M. Charron, L. Speak, and
15 B. Hansen, 2005: Atmospheric data assimilation with an ensemble Kalman filter:
16 Results with real observations. *Mon. Wea. Rev.*, **133**, 604–620.

17 Joly A., Jorgensen D., Shapiro M. A. et al, 1997: The Fronts and Atlantic Storm-Track
18 Experiment (FASTEX): scientific objectives and experimental design. *Bull. Amer.*
19 *Meteor. Soc.*, **78**, 1917–1940.

20 Kim, H., S. Kim, B. Jung, 2011: Real-time adaptive observation guidance using
21 singular vectors for typhoon Jangmi (200815) in T-PARC 2008. *Wea.*
22 *Forecasting*, **26**, 634–649.

- 1 Langland, R., and G. D., Rohaly, 1996: Adjoint-based Targeting of Observations for
2 FASTEX Cyclones. Pp. 369–371 in Proceedings of *Seventh Mesoscale Processes*
3 *Conference*, 9-13 September 1996, Reading, UK. American Meteorological
4 Society, Boston, USA.
- 5 Langland, R., 1999: Workshop on targeted observations for extratropical and tropical
6 forecasting. *Bull. Amer. Meteor. Soc.*, **80**, 2331–2338.
- 7 Langland, R., 2005: Issues in targeted observing. *Q. J. R. Meteorol. Soc.*, **131**,
8 3409–3425.
- 9 Liu, J., and E. Kalnay, 2008: Estimating observation impact without adjoint model in
10 an ensemble Kalman filter. *Q. J. R. Meteorol. Soc.*, **134**, 1327–1335.
- 11 Lu, J., and G. Chen, 1993: Some basic facts about the southwest China vortex and
12 their preliminary analysis. *Journal of Chengdu Institute of Meteorology*, **27(4)**,
13 7–15.
- 14 Majumdar, S. J., C. Bishop, B. Etherton, and Z. Toth, 2002a: Adaptive sampling with
15 the ensemble transform Kalman filter. II: Field program implementation. *Mon.*
16 *Wea. Rev.*, **130**, 1356–1369.
- 17 Majumdar, S. J., C. Bishop, R. Buizza, and R. Gelaro, 2002b: A comparison of
18 ensemble-transform Kalman-filter targeting guidance with ECMWF and NRL
19 total-energy singular vector guidance. *Q. J. R. Meteorol. Soc.*, **128**, 2527–2549.
- 20 Majumdar, S. J., S. Aberson, C. Bishop, R. Buizza, M. Peng, and C. Reynolds, 2006:
21 A comparison of adaptive observing guidance for Atlantic tropical cyclones. *Mon.*
22 *Wea. Rev.*, **134**, 2354–2372.

- 1 Mansfield, D., D. Richardson, and B. Truscott, 2005: An overview of the Atlantic
2 THORPEX Regional Campaign, A-TRec. In Proceedings of the THORPEX
3 Science Symposium, 6–10 December 2004, Montreal, Canada. World
4 Meteorological Organization, Geneva, Switzerland.
- 5 Mlawer, E. J., S. J. Taubman, P. D. Brown, M. J. Iacono, and S. A. Clough, 1997:
6 Radiative transfer for inhomogeneous atmosphere: RRTM, a validated
7 correlated-k model for the longwave. *J. Geophys. Res.*, **102 (D14)**,
8 16663–16682.
- 9 Meng, Z., and F. Zhang, 2007: Tests of an ensemble Kalman filter for mesoscale and
10 regional-scale data assimilation. Part II: Imperfect model experiments. *Mon. Wea.*
11 *Rev.*, **135**, 1403–1423.
- 12 Meng, Z., and F. Zhang, 2008a: Test of an ensemble Kalman Filter for mesoscale and
13 regional-scale data assimilation. Part III: Comparison with 3DVar for a real-data
14 case study. *Mon. Wea. Rev.*, **136**, 522–540.
- 15 Meng, Z., and F. Zhang, 2008b: Test of an ensemble Kalman Filter for mesoscale and
16 regional-scale data assimilation. Part IV: Comparison with 3DVar in
17 a month-long experiment. *Mon. Wea. Rev.*, **136**, 3671–3682.
- 18 Meng, Z., and F. Zhang, 2011: Limited-area ensemble-based data assimilation. *Mon.*
19 *Wea. Rev.*, **139**, 2025–2045.
- 20 Mu, M., W. Duan, and B. Wang, 2003: Conditional nonlinear optimal perturbation and
21 its applications, *Nonlinear Processes Geophys.*, **10**, 493–501.
- 22 Mu, M., F. Zhou, and H. Wang, 2009: A method for identifying the sensitive areas in

1 targeted observations for tropical cyclone prediction: conditional nonlinear
2 optimal perturbation, *Mon. Wea. Rev.*, **137**, 1623–1639.

3 Mu M., 2013: Methods, current status, and prospect of targeted observation. *Science*
4 *China: Earth Sciences*, **43(11)**, 1711-1725. doi: 10.1007/s11430-013-4727-x

5 Palmer, T., R. Gelaro, J. Barkmeijer, and R. Buizza, 1998: Singular vectors, metrics,
6 and adaptive observations. *J. Atmos. Sci.*, **55**, 633–653.

7 Parrish, D. F., and J. C. Derber, 1992: The National Meteorological Center’s spectral
8 statistical interpolation analysis system. *Mon. Wea. Rev.*, **120**, 1747–1763.

9 Pu, Z. X., E. Kalnay, J. Sela, and I. Szunyogh, 1997: Sensitivity of forecast errors to
10 initial conditions with a quasi-inverse linear method. *Mon. Wea. Rev.*, **125**,
11 2479–2503.

12 Qin, X., M. Mu, 2011: A study on the reduction of forecast error variance by three
13 adaptive observation approaches for tropical cyclone prediction. *Mon. Wea.*
14 *Rev.*, **139**, 2218–2232.

15 Reynolds C., and T. Rosmond, 2003: Nonlinear growth of singular-vector-based
16 perturbations, *Q. J. R. Meteor. Soc.*, **129**, 3059–3078.

17 Skamarock, W., and Coauthors, 2008: A description of the advanced research WRF
18 version 3. NCAR Tech. Note TN-475_STR, 113 pp.

19 Snyder C., 1996: Summary of a Workshop on Adaptive observation and FASTEX.
20 *Bull. Amer. Meteor. Soc.*, **77**, 953–961.

21 Szunyogh, I., Z. Toth, R. Morss, S. Majumdar, B. Etherton, and C. Bishop, 2000: The
22 effect of targeted dropsonde observations during the 1999 Winter Storm

- 1 Reconnaissance Program. *Mon. Wea. Rev.*, **128**, 3520–3537.
- 2 Tao S., and Y. Ding, 1981: Observational evidence of the influence of the
3 Qinghai-Xizang (Tibet) Plateau on the occurrence of heavy rain and severe
4 convective storms in China. *Bull. Amer. Meteor. Soc.* , **62**, 23–30.
- 5 Wu, C., and Coauthors, 2005: Dropwindsonde observations for typhoon surveillance
6 near the Taiwan region (DOTSTAR): An overview. *Bull. Amer. Meteor. Soc.*, **86**,
7 787–790.
- 8 Wu, C., K. Chou, P. Lin, S. Aberson, M. Peng and T. Nakazawa, 2007a: The impact of
9 dropwindsonde data on typhoon track forecasts in DOTSTAR. *Wea.*
10 *Forecasting*, **22**, 1157–1176.
- 11 Wu, C., J. Chen, P. Lin, K. Chou, 2007b: Targeted observations of tropical cyclone
12 movement based on the adjoint-derived sensitivity steering vector. *J. Atmos.*
13 *Sci.*, **64**, 2611–2626.
- 14 Wu, C. and Coauthors, 2009: Intercomparison of targeted observation guidance of
15 typhoon Shanshan (2006) with the midlatitude trough from both adjoint-derived
16 sensitivity steering vector and potential vorticity perspectives. *Mon. Wea. Rev.*,
17 **137**, 852–862
- 18 Wu, D., Z. Meng, and D. Yan, 2013: The predictability of a squall line in South
19 China on 23 April 2007. *Adv. Atmos. Sci.*, **30(2)**, 485–502.
- 20 Xie, B., F. Zhang, Q. Zhang, J. Poterjoy and Y. Weng, 2013: Observing strategy and
21 observation targeting for tropical cyclones using ensemble-based sensitivity
22 analysis and data assimilation. *Mon. Wea. Rev.*, **141**, 1437–1453

1 Yamaguchi, M., T. Iriguchi, T. Nakazawa, C. Wu, 2009: An observing system
2 experiment for typhoon Conson (2004) using a singular vector method and
3 DOTSTAR Data. *Mon. Wea. Rev.*, **137**, 2801–2816.

4 Zhang, F., C. Snyder, and R. Rotunno, 2003: Effects of moist convection on
5 mesoscale predictability. *J. Atmos. Sci.*, **60**, 1173–1185.

6 Zhang, F., Z. Meng, and A. Aksoy, 2006: Tests of an ensemble Kalman filter for
7 mesoscale and regional-scale data assimilation. Part I: Perfect model experiments.
8 *Mon. Wea. Rev.*, **134**, 722–736.

9

1 **Figure captions**

2 Fig. 1. The observed 24-h accumulated rainfall (0000 UTC 12 June – 0000 UTC 13 June 2008;
3 shaded). The heavy line represents the track of the MCV center at 12-h intervals. The names of
4 different provinces are also given in the figure for reference.

5
6 Fig. 2. Geopotential height [solid, 10 geopotential meters (gpm)] and temperature (dotted, every
7 2K) at 500 hPa, and relative vertical vorticity at 700 hPa (shaded, $10^{-5}s^{-1}$) at (a) 1200 UTC 10 June,
8 (b) 0000 UTC 11 June, (c) 1800 UTC 12 June, and (d) 0000 UTC 13 June. The white crosses in
9 (b)–(d) represent the center of the MCV.

10
11 Fig. 3. Geopotential height [red, 10 geopotential meters (gpm)], streamline (black), and relative
12 vertical vorticity at 700 hPa (gray shaded, $10^{-5}s^{-1}$) at (a) 1200 UTC 10 June, (b) 1800 UTC 10 June,
13 (c) 0000 UTC 11 June, (d) 1200 UTC 12 June, (e) 1800 UTC 12 June, and (f) 0000 UTC 13 June.
14 The black box in (c) indicates the area in which synthetic observations were generated and
15 assimilated in the OSSE. The white crosses in (c)–(f) represent the center of the MCV.

16
17 Fig. 4. Schematic flow chart of the piece-by-piece data assimilation targeting strategy.

18
19 Fig. 5. Model domains and their grid sizes in the numerical experiments.

20
21 Fig. 6. The streamline and relative vertical vorticity (left column, shaded, $10^{-5}s^{-1}$) at 700 hPa, the
22 composite radar reflectivity (middle column, dBZ) at 1800 UTC 12 June, and $RAIN_{24}$ (right
23 column, mm) in the (a) observation, (b) control experiment, (c) “truth”, and (d) M3, (e) M27, (f)
24 M6, and (g) M30. The white crosses in the left column indicate the location of the MCV center.

25
26 Fig. 7. Schematic representation of how the target area was determined with the R index of M27
27 of the ensemble as an example. The individual pieces are marked by white boundaries. The sides
28 connecting all the pieces are marked in orange. The white cross indicates the location of the MCV
29 center of the “truth” at the initial time.

30
31 Fig. 8. The evolution of the $DTEs$ of the 39 ensemble members (a) with respect to simulation time.
32 Panel (b) is the same as (a) but with six outlier members [black line in (a)] removed from the 39
33 members. The highlighted members were selected to examine the variability of the target area
34 with similar error evolution.

35
36 Fig. 9. The distribution of R index in the 33 members. The white crosses indicate the center of the
37 MCV of the “truth” at the initial time. The number in the lower-left corner of each panel is $N_p + N_s$,
38 and that in the lower-right corner is N_u . Members that have target area are denoted by the numbers
39 in black.

40
41 Fig. 10. The TSs and $DTEs$ in different experiments as well as the random distribution of data
42 units.

43

1 Fig. 11. The distribution of R index in the panels with “1” in their titles, F index in the panels with
2 “2” in their titles, I index in the panels with “3” in their titles (the number in the lower-left corner
3 of each panel is $N_p + N_s$, and that in the lower-right corner is N_u), error (an ensemble member
4 minus “truth”) of initial temperature (shaded; K) in the panels with “4” in their titles, vertical
5 vorticity (shaded; 10^{-5} s^{-1}) and horizontal wind speed (contour; m s^{-1}) in the panels with “5” in
6 their titles at 700 hPa, the vertically averaged DTE at the initial (0000 UTC 11 June, marked by
7 “6” in the title of the panels) and end time (0000 UTC 13 June, marked by “7” in the title of the
8 panels) of the integration time period for different members of (a) M3, (b) M27, (c) M6, and (d)
9 M30. The black box in panels with “6” in their titles indicates part of the square area in which
10 synthetic observations were generated and assimilated in the OSSE. The white crosses indicate the
11 location of the MCV center of the “truth” at the initial time.

12
13 Fig. 12. The mean (a) R , (b) F , and (c) I index over the 33 members. The white cross indicates the
14 center of the MCV of the “truth” at the initial time. The number in the lower-left corner of each
15 panel is $N_p + N_s$, and that in the lower-right corner is N_u .

16
17 Fig. 13. The distribution of F index in the 33 members. The white crosses indicate the center of
18 the MCV of the “truth” at the initial time. The number in the lower-left corner of each panel is N_p
19 $+ N_s$, and that in the lower-right corner is N_u . Members that have target area are denoted by the
20 numbers in black.

21
22 Fig. 14. The distribution of I index in the 33 members. The white crosses indicate the center of the
23 MCV of the “truth” at the initial time. The number in the lower-left corner of each panel is $N_p + N_s$,
24 and that in the lower-right corner is N_u . Members that have target area are denoted by the numbers
25 in black.

26

1 **Tables**

2 Table 1. Default observation error of wind profiler in WRF-3DVar.

Pressure (hPa)	1000	900	850	800	750	700	650	600	550
Error (m s ⁻¹)	2.2	2.2	2.2	2.2	2.2	2.2	2.4	2.6	2.7
Pressure (hPa)	500	450	400	350	300	250	200	150	100
Error (m s ⁻¹)	2.8	2.9	3.0	3.1	3.2	3.1	3.0	2.8	2.8

3

4

5

6

7 Table 2. The compactness and variability of target areas and the percentage of the ensemble with
8 target areas for forecasted rainfall, initial and forecasted total energy.

9

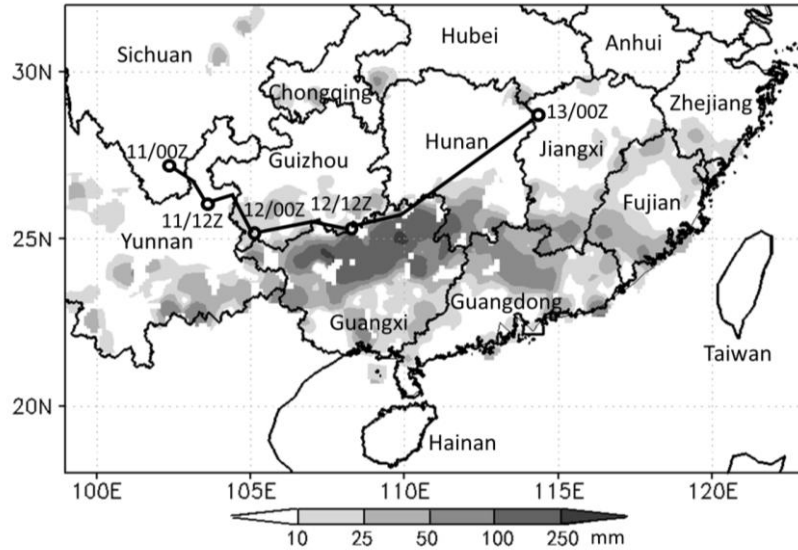
	<i>RAIN</i> ₂₄	Forecast total energy	Initial total energy
Mean of $N_p + N_s$	5.4	3.2	1.9
STD of $N_p + N_s$	6.3	3.4	2.1
Percentage with target area	45%	64%	76%

10

11

1 **Figures**

2
3
4

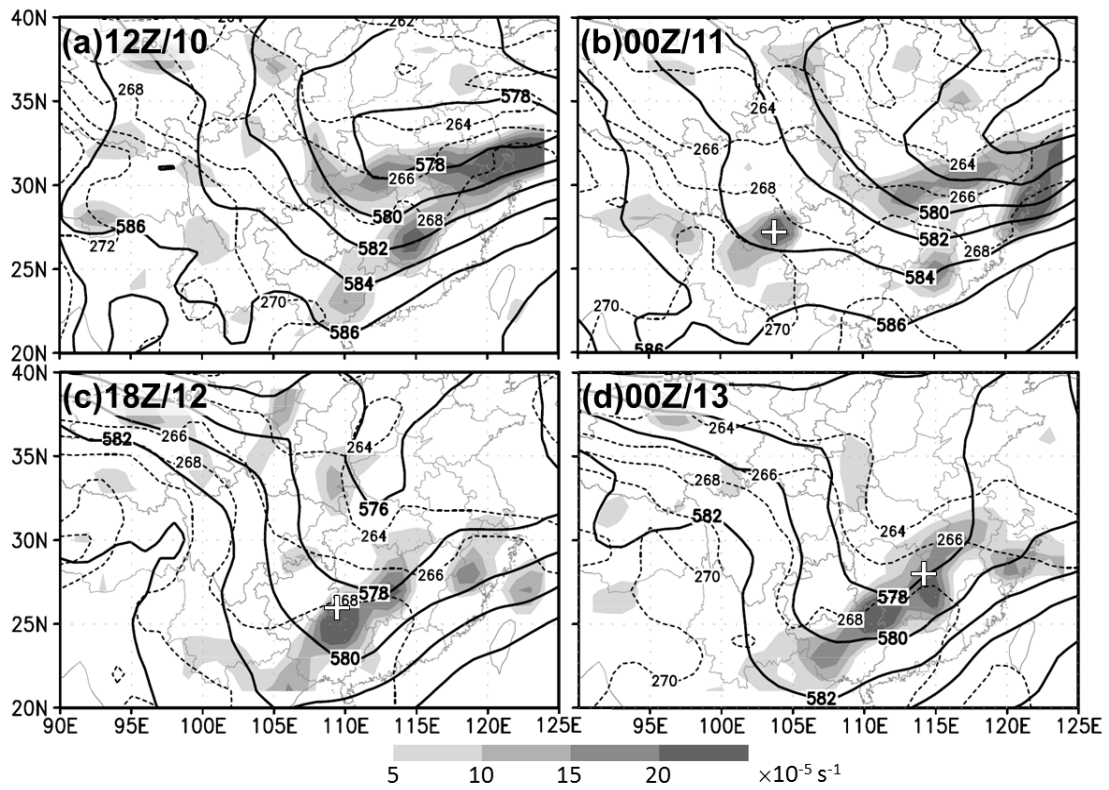


5
6

7 Fig. 1. The observed 24-h accumulated rainfall (0000 UTC 12 June – 0000 UTC 13 June 2008;
8 shaded). The heavy line represents the track of the MCV center at 12-h intervals. The names of
9 different provinces are also given in the figure for reference.

10
11
12
13
14
15
16
17
18
19
20
21
22
23
24
25
26

1

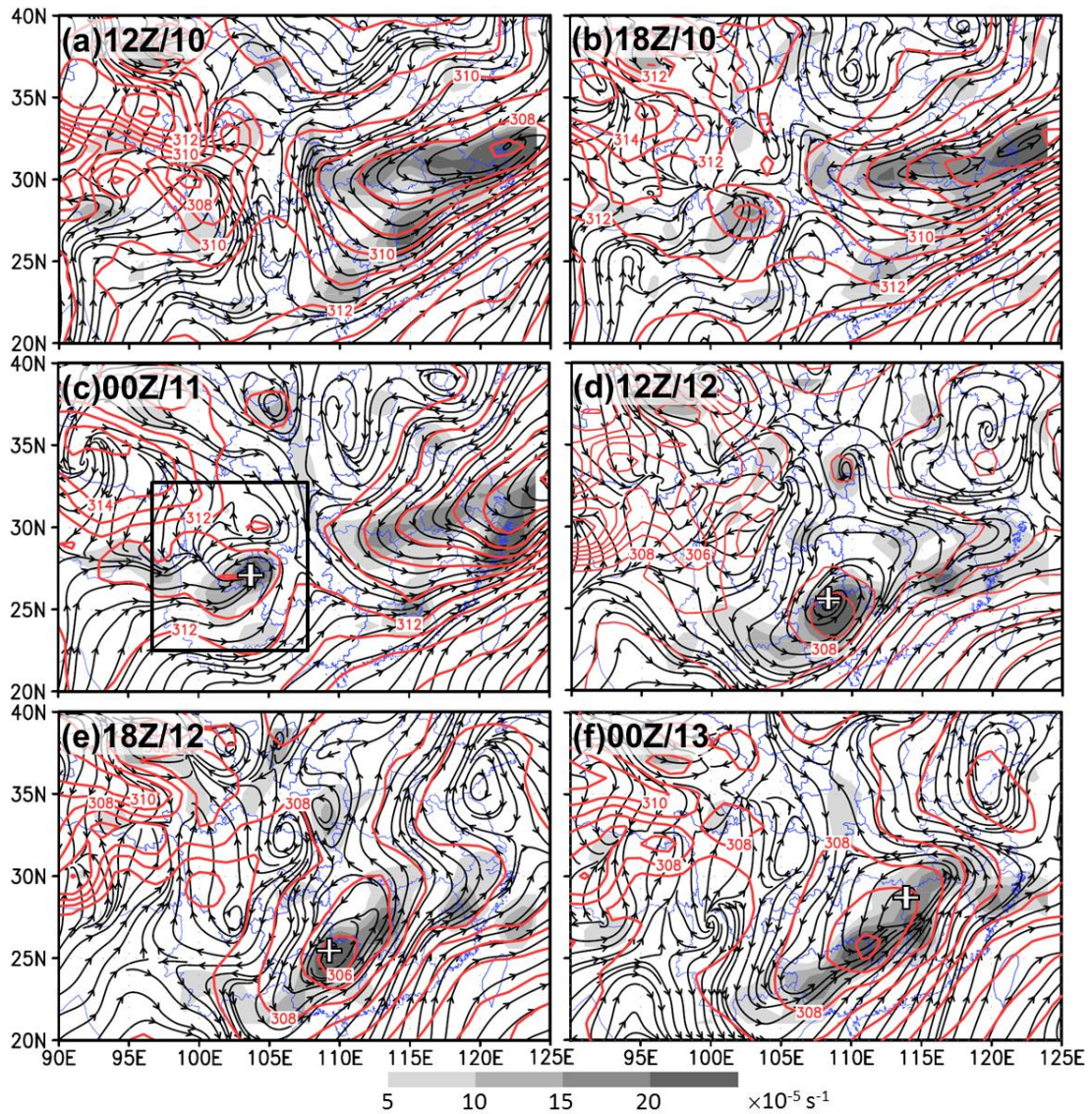


2

3 Fig. 2. Geopotential height [solid, 10 geopotential meters (gpm)] and temperature (dotted, every
4 2K) at 500 hPa, and relative vertical vorticity at 700 hPa (shaded, 10^{-5} s^{-1}) at (a) 1200 UTC 10 June,
5 (b) 0000 UTC 11 June, (c) 1800 UTC 12 June, and (d) 0000 UTC 13 June. The white crosses in
6 (b)–(d) represent the center of the MCV.

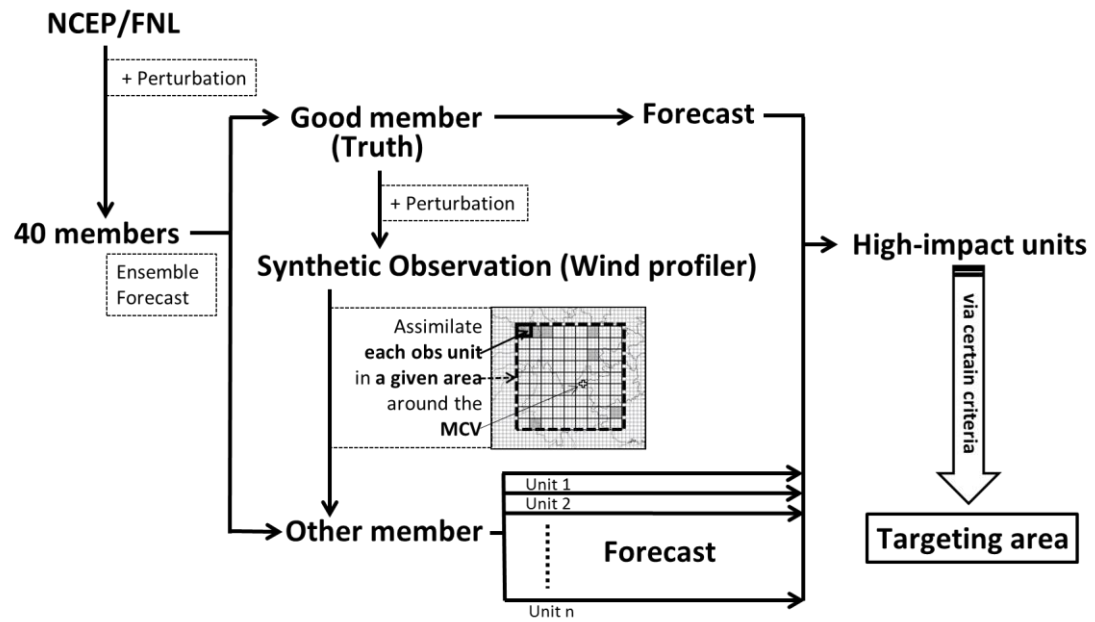
7

1
2



3
4
5
6
7
8
9
10
11

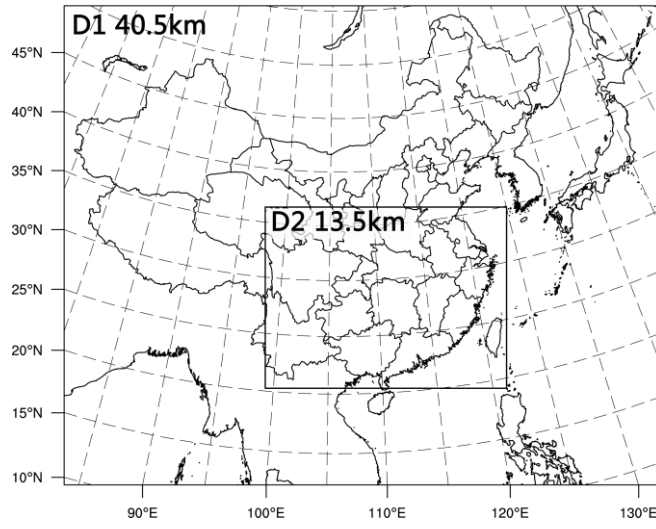
Fig. 3. Geopotential height [red, 10 geopotential meters (gpm)], streamline (black), and relative vertical vorticity at 700 hPa (gray shaded, 10^{-5} s^{-1}) at (a) 1200 UTC 10 June, (b) 1800 UTC 10 June, (c) 0000 UTC 11 June, (d) 1200 UTC 12 June, (e) 1800 UTC 12 June, and (f) 0000 UTC 13 June. The black box in (c) indicates the area in which synthetic observations were generated and assimilated in the OSSE. The white crosses in (c)–(f) represent the center of the MCV.



1
2
3
4
5
6
7
8

Fig. 4. Schematic flow chart of the piece-by-piece data assimilation targeting strategy.

1



2

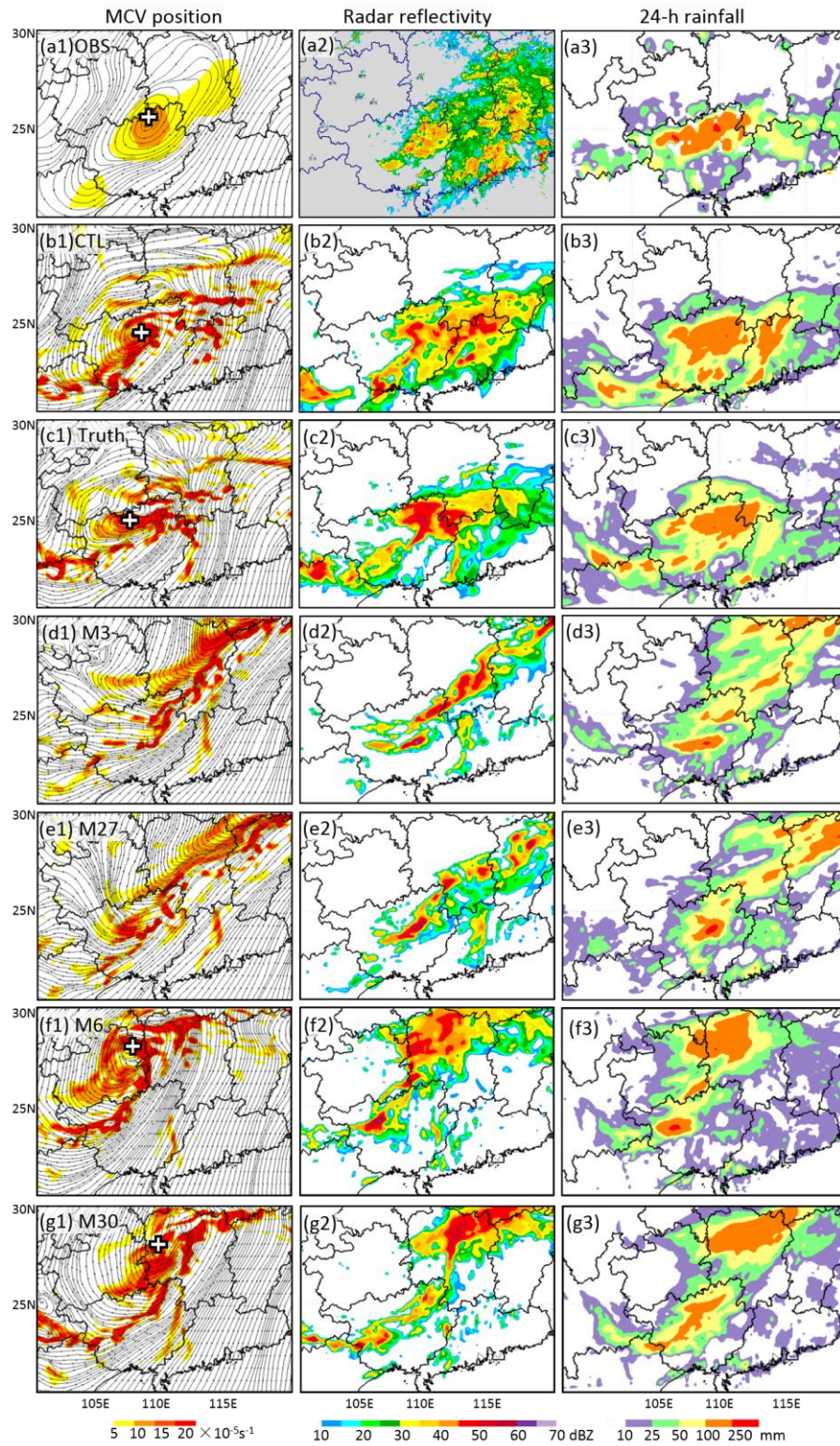
3

4

5

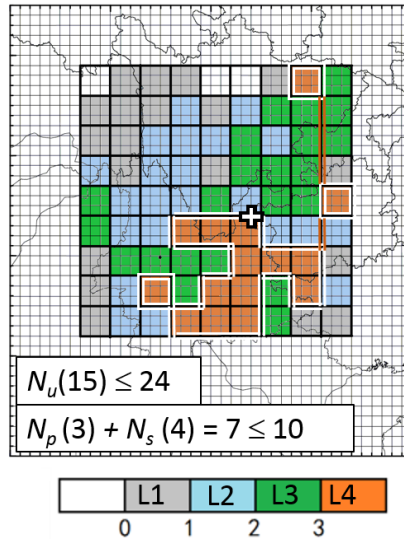
6

Fig. 5. Model domains and their grid sizes in the numerical experiments.

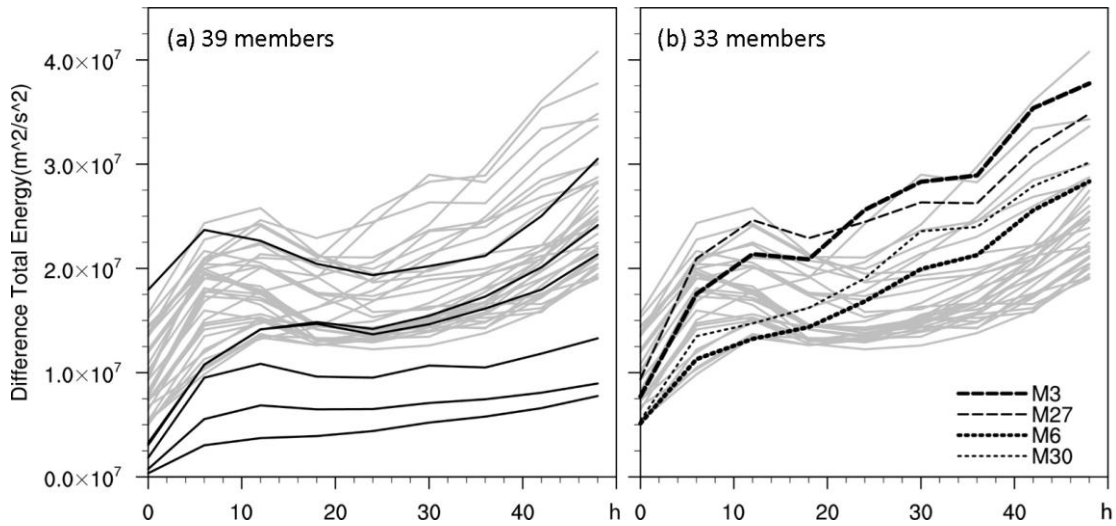


1
2
3
4
5
6

Fig. 6. The streamline and relative vertical vorticity (left column, shaded, $10^{-5} s^{-1}$) at 700 hPa, the composite radar reflectivity (middle column, dBZ) at 1800 UTC 12 June, and $RAIN_{24}$ (right column, mm) in the (a) observation, (b) control experiment, (c) “truth”, and (d) M3, (e) M27, (f) M6, and (g) M30. The white crosses in the left column indicate the location of the MCV center.



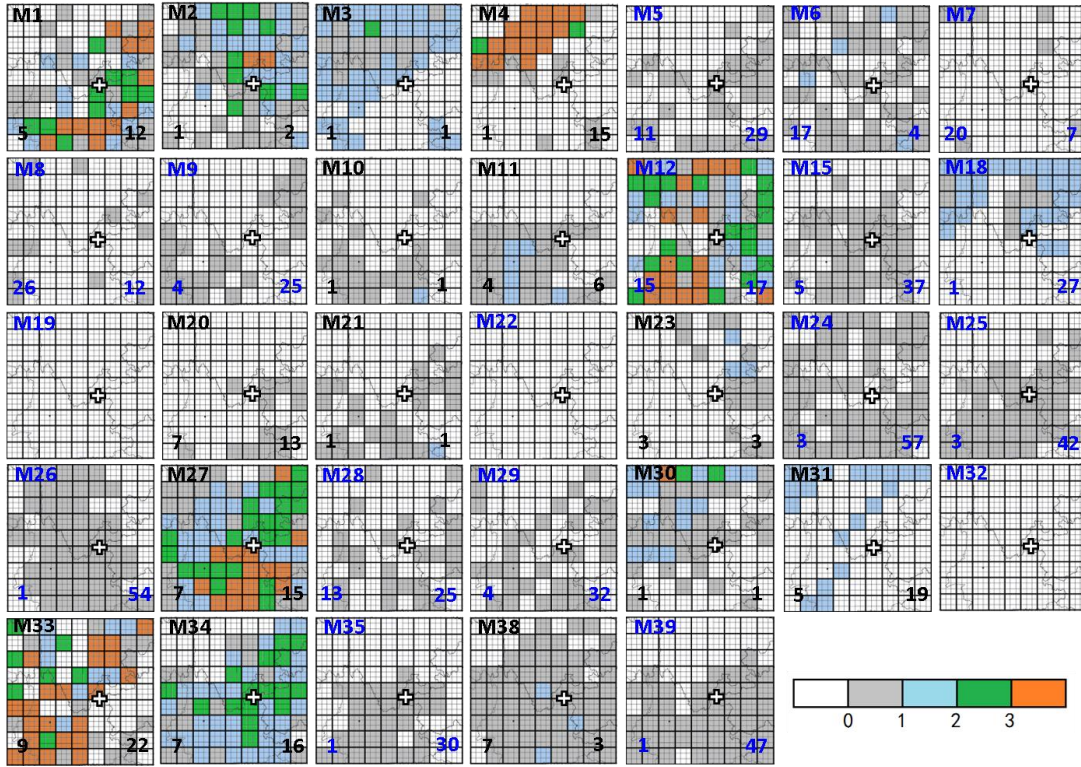
1
 2 Fig. 7. Schematic representation of how the target area was determined with the R index of M27
 3 of the ensemble as an example. The individual pieces are marked by white boundaries. The sides
 4 connecting all the pieces are marked in orange. The white cross indicates the location of the MCV
 5 center of the “truth” at the initial time.



1
2
3
4
5
6
7
8

Fig. 8. The evolution of the *DTEs* of the 39 ensemble members (a) with respect to simulation time. Panel (b) is the same as (a) but with six outlier members [black line in (a)] removed from the 39 members. The highlighted members were selected to examine the variability of the target area with similar error evolution.

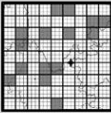
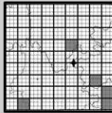
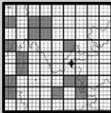
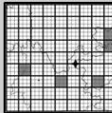
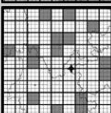
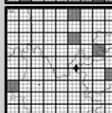
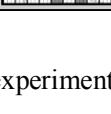
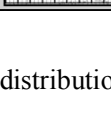
1
2
3
4
5
6



7
8
9
10
11
12
13
14
15
16
17
18
19

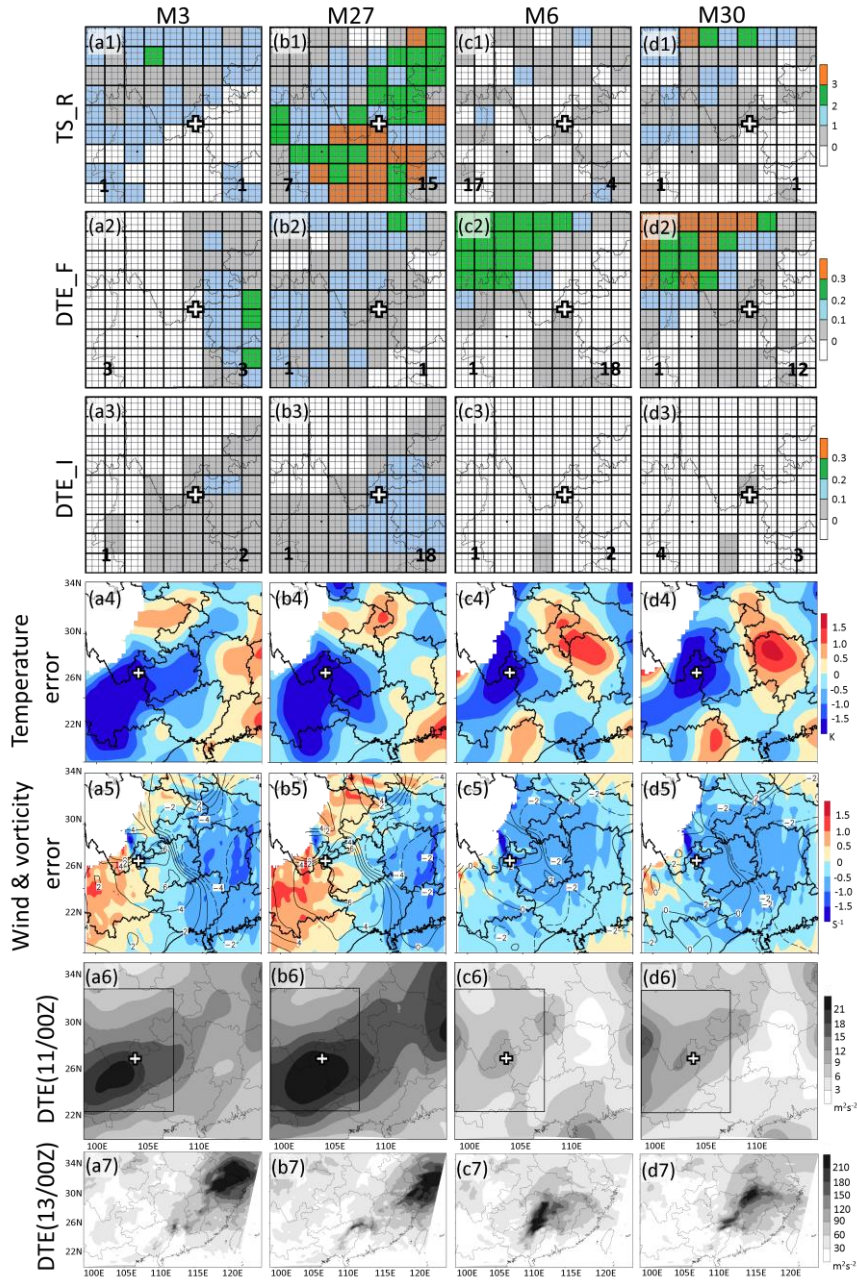
Fig. 9. The distribution of R index in the 33 members. The white crosses indicate the center of the MCV of the “truth” at the initial time. The number in the lower-left corner of each panel is $N_p + N_s$, and that in the lower-right corner is N_u . Members that have target area are denoted by the numbers in black.

1
2
3
4

	M27		Ensemble Mean		
	<i>TS</i>	Random distribution	<i>DTE</i> (m ² /s ²)	<i>TS</i>	Random distribution
NoDA	0.02	1 	36.93	0.10	1 
Target area for rainfall	0.11				
Target area for total energy		3 	33.99	0.11	3 
Random1	0.08				
Random2	0.07	5 	33.83	0.09	5 
Random3	0.06				
Random4	0.09	33.83	0.09		
Random5	0.08			5 	5 
Random media	0.08				

5
6
7
8
9

Fig.10 The *TSs* and *DTEs* in different experiments as well as the random distribution of data units.

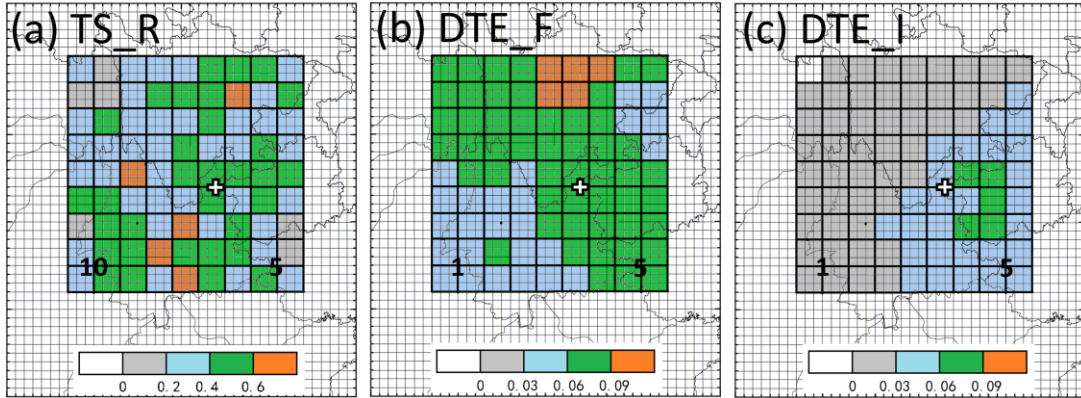


1

2 Fig. 11. The distribution of R index in the panels with “1” in their titles, F index in the panels with
 3 “2” in their titles, I index in the panels with “3” in their titles (the number in the lower-left corner
 4 of each panel is $N_p + N_s$, and that in the lower-right corner is N_u), error (an ensemble member
 5 minus “truth”) of initial temperature (shaded; K) in the panels with “4” in their titles, vertical
 6 vorticity (shaded; 10^{-5} s^{-1}) and horizontal wind speed (contour; m s^{-1}) in the panels with “5” in
 7 their titles at 700 hPa, the vertically averaged DTE at the initial (0000 UTC 11 June, marked by
 8 “6” in the title of the panels) and end time (0000 UTC 13 June, marked by “7” in the title of the
 9 panels) of the integration time period for different members of (a) M3, (b) M27, (c) M6, and (d)
 10 M30. The black box in panels with “6” in their titles indicates part of the square area in which
 11 synthetic observations were generated and assimilated in the OSSE. The white crosses indicate the
 12 location of the MCV center of the “truth” at the initial time.

13

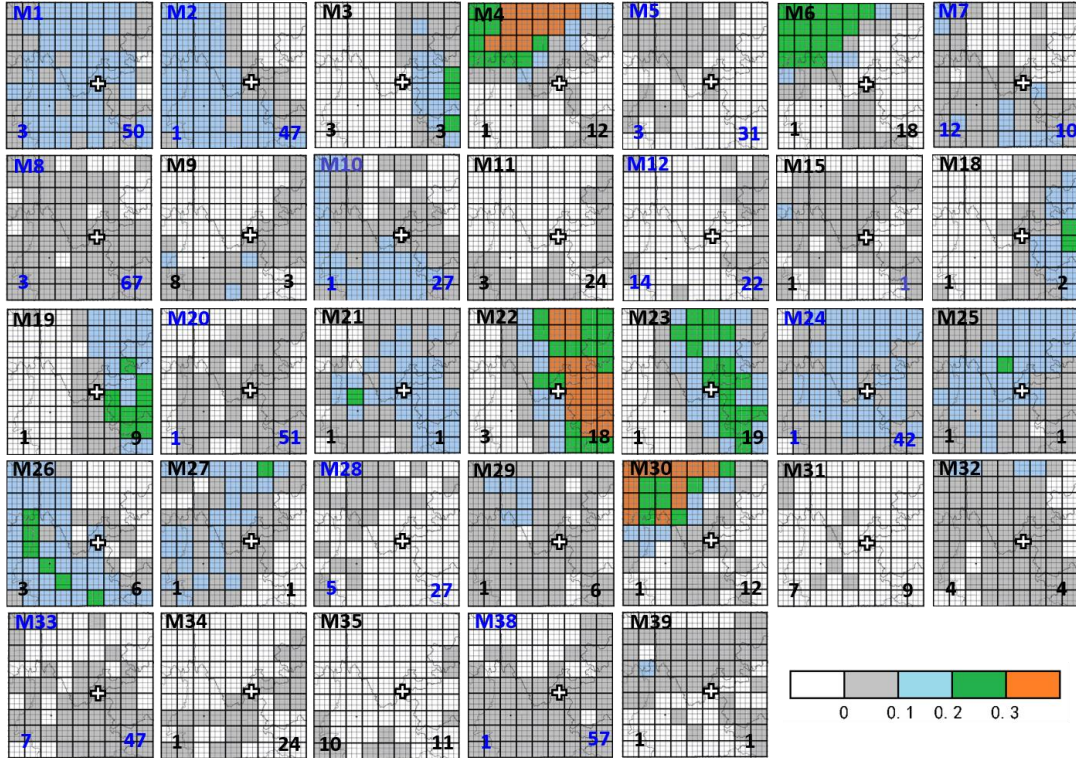
1
2
3
4
5



6
7
8
9
10
11
12

Fig. 12. The mean (a) R , (b) F , and (c) I index over the 33 members. The white cross indicates the center of the MCV of the “truth” at the initial time. The number in the lower-left corner of each panel is $N_p + N_s$, and that in the lower-right corner is N_u .

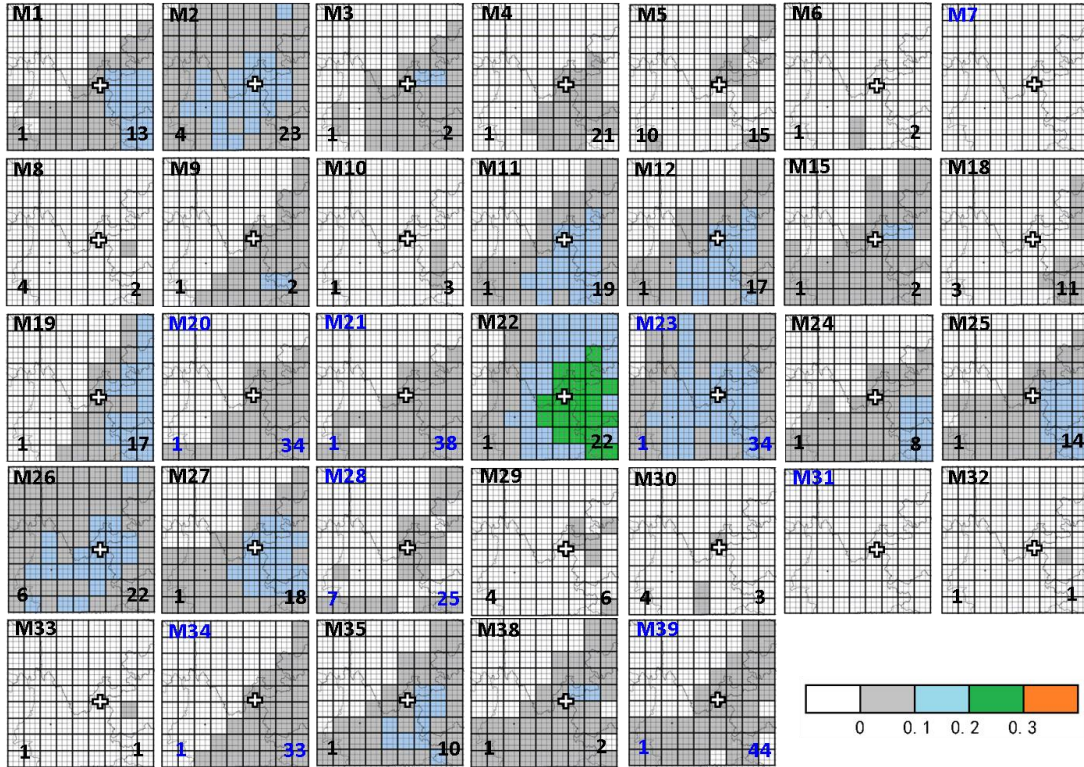
1
2
3
4
5



6
7
8
9
10
11
12
13
14

Fig. 13. The distribution of F index in the 33 members. The white crosses indicate the center of the MCV of the “truth” at the initial time. The number in the lower-left corner of each panel is $N_p + N_s$, and that in the lower-right corner is N_u . Members that have target area are denoted by the numbers in black.

1
2
3
4
5



6
7
8
9
10
11
12
13
14

Fig. 14. The distribution of I index in the 33 members. The white crosses indicate the center of the MCV of the “truth” at the initial time. The number in the lower-left corner of each panel is $N_p + N_s$, and that in the lower-right corner is N_u . Members that have target area are denoted by the numbers in black.